

T-type cell mediated photoacoustic spectroscopy for simultaneous detection of multi-component gases based on triple resonance modality

Le Zhang^a, Lixian Liu^a, Xueshi Zhang^a, Xukun Yin^a, Huiting Huan^a, Huanyu Liu^a, Xiaoming Zhao^a, Yufei Ma^b, Xiaopeng Shao^{a,*}

^a School of Optoelectronic Engineering, Xidian University, Xi'an 710071, China

^b National Key Laboratory of Science and Technology on Tunable Laser, Harbin Institute of Technology, Harbin 150001, China

ARTICLE INFO

Keywords:

Photoacoustic spectroscopy
Multi-gas sensing
T-type photoacoustic cell
Multi-resonance excitation
Frequency division multiplexing

ABSTRACT

Enhancing multi-gas detectability using photoacoustic spectroscopy capable of simultaneous detection, highly selectivity and less cross-interference is essential for dissolved gas sensing application. A T-type photoacoustic cell was designed and verified to be an appropriate sensor, due to the resonant frequencies of which are determined jointly by absorption and resonant cylinders. The three designated resonance modes were investigated from both simulation and experiments to present the comparable amplitude responses by introducing excitation beam position optimization. The capability of multi-gas detection was demonstrated by measuring CO, CH₄ and C₂H₂ simultaneously using QCL, ICL and DFB lasers as excitation sources respectively. The influence of potential cross-sensitivity towards humidity have been examined in terms of multi-gas detection. The experimentally determined minimum detection limits of CO, CH₄ and C₂H₂ were 89ppb, 80ppb and 664ppb respectively, corresponding to the normalized noise equivalent absorption coefficients of $5.75 \times 10^{-7} \text{ cm}^{-1} \text{ W Hz}^{-1/2}$, $1.97 \times 10^{-8} \text{ cm}^{-1} \text{ W Hz}^{-1/2}$ and $4.23 \times 10^{-8} \text{ cm}^{-1} \text{ W Hz}^{-1/2}$.

1. Introduction

Oil-immersed power transformer is one of the most important insulation equipment in modern power distribution and transmission systems. Simultaneous measurements of the dissolved gases in insulating oil, such as carbon monoxide (CO), methane (CH₄) and acetylene (C₂H₂), can represent a suitable solution in early diagnosis of overheating, arcing and partial discharge failures of power transformers [1–3]. Transformer fault can mainly be divided into overheating fault and discharge fault. The content changes of CO, CH₄, and C₂H₂ are the main indicators of transformer failure. Overheating fault includes bare metal overheating, solid insulation overheating and low temperature overheating. The bare metal overheating is characterized by the rising concentration of hydrocarbon gas, such as CH₄ and C₂H₄. The sum of the above two gases accounts for more than 80% of the total hydrocarbon gas, and CH₄ accounts for a larger proportion (>30 ppm). The concentration of CO (>300 ppm) strongly indicates the solid insulation overheating and the low temperature overheating in the transformer failure. When the transformer is in discharge fault, the C₂H₂ will increase dramatically (>5 ppm, 20%–70% of the total hydrocarbon gas) [4].

Therefore, CO, CH₄, and C₂H₂ are selected as the target analytes in this work.

The traditional quantitative detection of multiple analytes, such as gas chromatographs, semiconductor gas sensors and electrochemical sensors, were limited in terms of real time monitoring, recovery time, poor selectivity and cross sensitivity [5]. Photoacoustic spectroscopy (PAS)-based optical sensor platforms [6–11], which feature the advantages of high sensitivity, high selectivity, fast response, long lifetime and well-established sensing devices, have played an important role in the field of multi-component gas sensing [12–18]. Various PAS-based multi-gas sensor modalities have been developed, such as Fourier transform infrared PAS modality [19,20], broadband detection based thermal emitters or blackbody radiators using several band-pass filters [21], the use of multi-lasers combined time-division multiplexing (TDM) methods [22–24], and multi-resonators with frequency-division multiplexing (FDM) schemes [25]. Due to the relatively poor intensity of the broadband source, the weak photoacoustic (PA) signals were sensitively affected by the background noise, which was a major obstacle to highly sensitive detection [26]. The use of multiple lasers with TDM technology needed to drive the laser sources by sending the modulation signals of

* Corresponding author.

E-mail address: xpshao@xidian.edu.cn (X. Shao).

<https://doi.org/10.1016/j.pacs.2023.100492>

Received 30 October 2022; Received in revised form 31 March 2023; Accepted 11 April 2023

Available online 12 April 2023

2213-5979/© 2023 Published by Elsevier GmbH. This is an open access article under the CC BY-NC-ND license (<http://creativecommons.org/licenses/by-nc-nd/4.0/>).

different frequencies in time sequence, or to alternately switch the excitation lasers. In this case, the measurement of multiple analytes cannot be performed at the same time, which limited the time resolution and the simultaneous detection capability. Generally, a single detector cannot distinguish the acoustic signals produced by different gas molecules at the same resonant frequency. The FDM technology can demodulate PA signals in different frequency modes without beam coupling and separation. However, multi-resonator structure composed of cylindrical cavities of different sizes resulted in bulky devices, which had complex manufacturing process and increased miniaturization difficulty [27]. Meanwhile, the use of acoustic guide tube would cause energy loss.

Therefore, utilizing a single PA cell (PAC) coupled with a single microphone can be an effective approach for simultaneous multi-gas sensing, avoiding acoustic coupling of multiple resonators and the increased optical elements required for laser beam alignment. H. Wu et al. [28] combined the overtone vibration mode of the quartz tuning fork (QTF) with the fundamental vibration mode to provide simultaneous dual-gas quartz-enhanced PAS detection using the FDM technique. A dual-gas quartz-enhanced photoacoustic (QEPAS) sensor capable of simultaneous detection of water vapor and alternatively methane or nitrous oxide was reported [29]. Q. Huang et al. [30] designed a spherical PAC with multiple resonance modes, and evaluated the capability for multi-component gas species analysis. However, the less resonance modes and amplitude response differences in magnitudes (more than 6 times) of resonant frequencies, which are intrinsic property of the existing single-cavity cells or QTFs, resulted in large differences in the detection precision for multi-component gases.

To overcome the problems of cylindrical longitudinal resonance modes and frequency response differences, a T-type PAC with three resonant frequencies was designed and employed for simultaneous detection of CO, CH₄ and C₂H₂ in this paper. The resonance modes were increased by adding the buffer cavities to change PA field distribution, and the acoustic sensitivity differences in various resonant frequencies were compensated by adjusting the vertical resonance cylinders. The incident excitation beams were optimized to irradiate to positions of T-type PAC for multiple resonance modes, which were verified by simulation and experimental investigation. A fixed concentration of water (H₂O) vapor was added in the PAS sensor system to increase the vibrational-translational (V-T) relaxation rates of CO molecules. This configuration of utilizing a single PAC and a single microphone can break through the limitations existing in previous multi-gas sensors, and result in an effective sensor architecture.

2. Methods

2.1. Absorption cross-section characteristic analysis and laser source selection

Validation of the developed multi-wavelength and multi-resonance PAS-based sensor was carried out by the measurements of three typical dissolved gases of CO, CH₄ and C₂H₂. The selected absorption cross-sections are given in Fig. 1, according to the HITRAN (2020) database [31]. The peak absorption coefficient was determined by simulation of the HITRAN data for a pressure of 1 atm. at 296 K. Quantitative measurements of CO in the ν_1 fundamental rotational vibrational band located at 2176.3 cm⁻¹ were carried out using a distributed feedback (DFB) quantum cascade laser (QCL). H₂O vapor has less absorption lines in this spectral band, and would not cause spectral interference for CO detection. A DFB interband cascade laser (ICL) emitting at 3.37 μ m was implemented as the excitation light source to target the asymmetric stretching vibration ν_3 CH₄ band in the MIR spectral range from 2968 cm⁻¹ to 2970 cm⁻¹. Then several weak absorption lines of H₂O vapor were found in the ICL tuning range from 2960 cm⁻¹ to 2972 cm⁻¹, which could cause spectral interference in subsequent experiments. The DFB laser diode operating at 6578.6 cm⁻¹ in the NIR band with a narrow linewidth of 2 MHz was chosen to excite the C₂H₂ molecules. These devices can also provide about single mode operation, laser modulation capability, low source noise and low amplitude fluctuations for highly sensitive and selective PAS applications.

2.2. Design and finite element analysis of the T-type PAC

The conventional H-type cylindrical PAC has fewer available resonance modes, and the acoustic sensitivity responses vary greatly at different resonant frequencies. These are inherent characteristics of the single-cylinder structure, which are not suitable for the simultaneous detection of multiple analytes [32]. The T-type longitudinal resonant PAC, which can be regarded as an extension of the Helmholtz resonator composed of absorption and resonance cylinders, takes the advantages of fast response time, high PAC constant, and simple manufacturing process [33,34]. Due to the perpendicular structure of T-type PAC, the acoustic sensitivities and resonant frequencies of different order resonance modes are mainly determined by the length of the vertical resonant cylinder [35,36]. The T-type PAC structure can be expected to realize simultaneous detection of multiple gases by multi-frequency responses. To suppress ambient noise and balance frequency responses in different modes, two buffer cavities were further added at both ends of the absorption cavity.

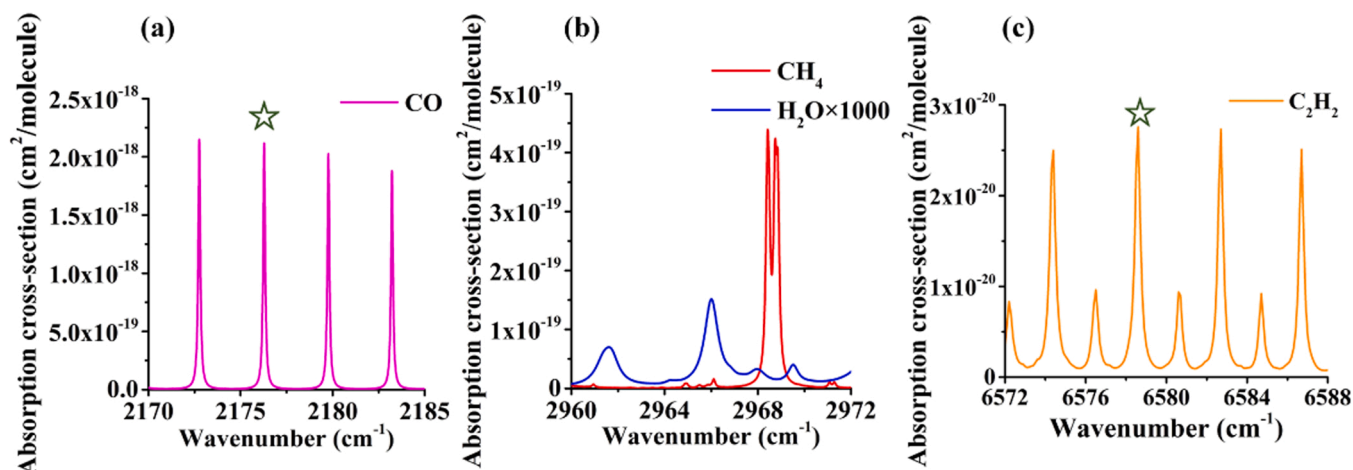


Fig. 1. Simulated spectral distribution characteristics of CO, CH₄ and C₂H₂ based on HITRAN Database. Temperature and pressure: 296 K and 1 atm respectively.

By comprehensively considering the resonant frequency responsiveness, the sizes of the resonant cavity and the buffer cavities were jointly optimized to compensate the acoustic sensitivity differences among resonance modes. The schematic of the home-made T-type PAC is shown in Fig. 2. This T-type PAC consists of a vertical resonant cavity with dimensions of 45 mm length and 8 mm diameter, a horizontal absorption cavity with dimensions of 60 mm length and 10 mm diameter, in addition two buffer cavities with 40 mm length and 44 mm diameter were set on both ends of the absorption cavity. The PAC was made of stainless steel with two calcium fluoride (CaF_2) windows located at the ends of the buffer cavities for incident light beam. A single microphone was placed in the top of the resonant cavity for PA signal detection. Compared with the H-type cylindrical PACs, this T-type PAC has the lower resonance frequency and more measurement modes, which are helpful for compactness and miniaturization in limited spaces [37].

Finite element analysis (FEA) of the developed T-type PAC with COMSOL Multiphysics 6.0 was employed to evaluate the resonance modes in various frequencies. Thermo-viscous acoustic interface was used to obtain the accurate acoustic characteristics of PAC. Fig. 3 shows the simulated sound pressure distribution of the three selected longitudinal resonance modes (F1, F2, and F3) at different frequencies (corresponding to the second-, third- and sixth-order resonance modes in simulation) of T-type PAC. In the FEA model, the temperature and the pressure were set at 298.15 K (25 °C) and 1 atm respectively. The used material of the gas sample was N_2 . As a criterion for selecting these resonance modes to achieve multi-gas simultaneous detection, the antinodes of the standing waves at different frequencies are always located at the end of the resonant cavity, where the maximum sound pressure exists. The resonant frequencies obtained from the simulation were about 1515 Hz (F1), 2962 Hz (F2) and 5625 Hz (F3), respectively. According to the FEA simulation, the Q factors and full widths at half maximum (FWHMs) of the resonance curves of F1, F2 and F3 can be calculated as $Q_1 = 31.6$, $\text{FWHM}_1 = 48$ Hz; $Q_2 = 70.5$, $\text{FWHM}_2 = 42$ Hz; and $Q_3 = 68.6$, $\text{FWHM}_3 = 82$ Hz.

Conventional PAS technology tends to pass the incident beam through the PACs to obtain the maximum optical absorption path, which can improve the signal to noise ratio (SNR). J. M. Rey et al. [38–40] have demonstrated that the PA amplitude ratios varied with the excitation beam positions based on differential mode excitation technique. This phenomenon that the sound pressure amplification gain changes with the optimization of excitation beam position is based on the principle of Helmholtz amplification and changed acoustic impedance [28]. Therefore, our developed T-type PAC can also improve the acoustic performance by optimizing the incident excitation beam position. As shown in Fig. 4(a) and (b), two incident ways of the excitation beam, which represent the heat source domains that generate sound waves in COMSOL simulation, are presented to explore the PA coupling optimization. The simulation results of the sound pressure vs. frequency for the three

selected resonance modes of T-type PAC are shown in Fig. 4(c)–(e). For F1 mode at 1515 Hz, the second excitation method only excited the PA signals in one of the buffers without the maximum absorption optical path, resulting in a larger sound pressure than that of the first incident way. This phenomenon did not exist in F2 and F3 mode results. The reason is that the Helmholtz amplification is related to the acoustic wavelength [41]. The condition for acoustic Helmholtz amplification requires that the acoustic wavelength is comparable with the dimensions of the resonator. Since rising the frequency, the acoustic wavelength will be shorter. The higher frequencies of F2 and F3 modes cannot produce Helmholtz amplification. The acoustic amplification at the resonant frequency depends on the losses (viscous and thermal losses) on the walls of the Helmholtz resonator. The theories of the acoustic amplification and the PA Helmholtz detector sensitivity are detailed in Ref. [40]. When the hole depth and aperture of the cavity were much smaller than the acoustic wave wavelength, the air column of the cavity was equivalent to a mass block. As the cavity volume was much larger than the aperture at Helmholtz resonant frequency, the effect of acoustic amplification was equivalent to the air spring, resulting in a "resonance–spring and mass block system" [32]. When the air plug in the buffer moves outward the pressure inside the cavity decreases, resulting in an inward-directed force, which tries to restore the original state.

3. Experimental setup

A schematic diagram of PAS-based multi-component gas sensor configuration equipped with the developed T-type PAC is shown in Fig. 5. Three excitation laser sources, including a DFB ICL (HealthyPhoton, model HPQCL-Q), a DFB QCL (HealthyPhoton, model QC-Qube) and an NIR laser diode (NEL) emitting at 2968 cm^{-1} , 2176.3 cm^{-1} and 6578.6 cm^{-1} , were employed to realize the simultaneous detection of CH_4 , CO and C_2H_2 . The optical powers of the ICL, QCL and NIR laser diode measured by a thermal power meter (Ophir Optronics 3 A) at the target absorption lines were 8 mW, 44 mW and 32 mW, respectively. All the laser sources were driven by tuning the current and temperature control. The two MIR sources have been collimated and packaged, and the NIR laser diode was collimated by the optical fiber collimator. All the measurements were performed in 2f-wavelength modulation spectroscopy (WMS) technique. To simultaneously detect the PA signals of CH_4 , CO and C_2H_2 , the three lasers were modulated by sinusoidal signals to match with half of the three resonance frequencies of the T-type PAC, respectively. A low-frequency triangular wave with 0.03 Hz was used to perform spectral scans and to realize the laser wavelength tuning and PA spectra acquisition. All the digital triangular ramp and sinusoidal modulation signals were generated by waveform generators (Tektronix, model AFG3021C). In particular, the QCL was radiated to the buffer cavity wall to excite CO molecules for F1 detection, while the ICL and NIR laser diode were transmitted along the axial center of the PAC to excite CH_4 and C_2H_2 for F2 and F3 detection. These beam positions can also be exchanged according to the detection sensitivity required for practical applications.

For the gas path, the system was composed of certified concentration gas cylinders, a mass flow controller (MFC), a humidifier, a flow meter, a system of needle valves and a vacuum pump. The sensor calibrations were performed using the following certified concentrations: 100 ppm CH_4/N_2 , 1000 ppm CO/N_2 and 100 ppm $\text{C}_2\text{H}_2/\text{N}_2$. The sample gas cylinders were connected to the inlet of the MFC, together with a cylinder containing pure nitrogen for successive dilutions. The MFC (MCQ Instruments, model Gas Blender 100 plus) was used to mix the gas sample ratios and to set a total flow rate of 400 standard cubic centimeters per minute (sccm). A humidifier was placed after the gas mixer to humidify the gas samples, fixing the water vapor concentration for all measurements. The unchanged humidity can avoid the various cross sensitivities in the gas mixtures, and can promote the V-T relaxation rates of CO molecules. Before entering the PAC, the humidified gases passed through a flow meter (ALICAT, model LLF4), which was employed to

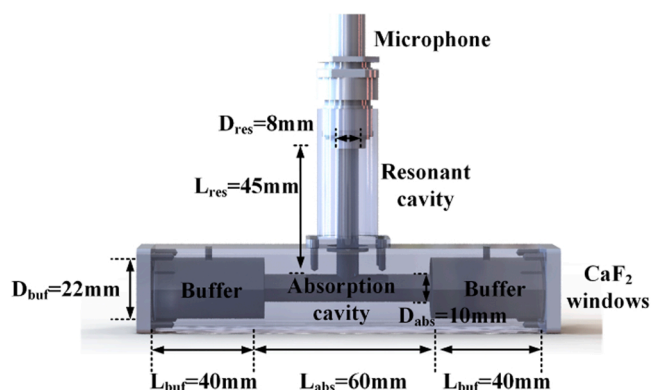


Fig. 2. Schematic structure of the developed T-type PAC.

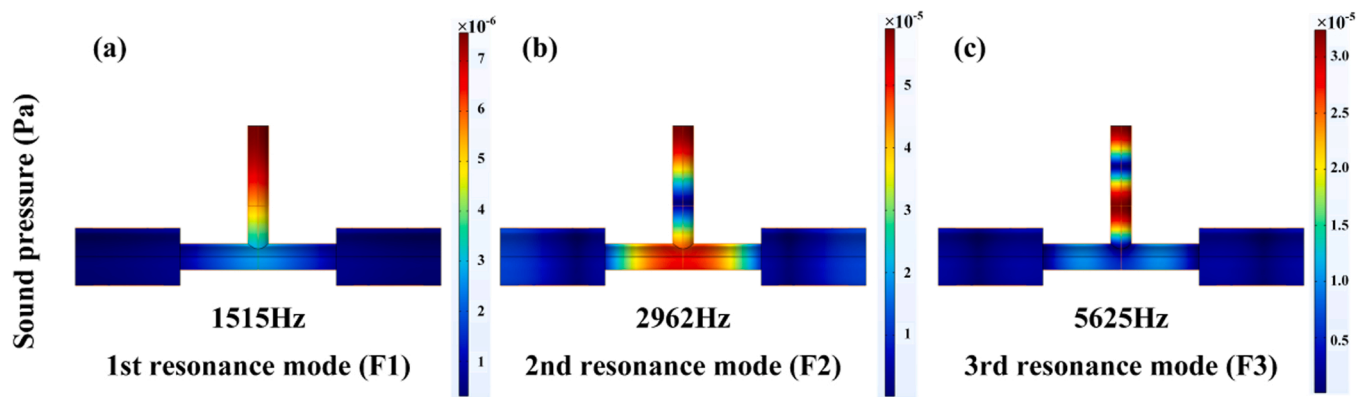


Fig. 3. Simulated sound pressure distribution of T-type PAC model for the three selected resonance modes by FEA method. Color bar: Simulated sound pressure (Pa).

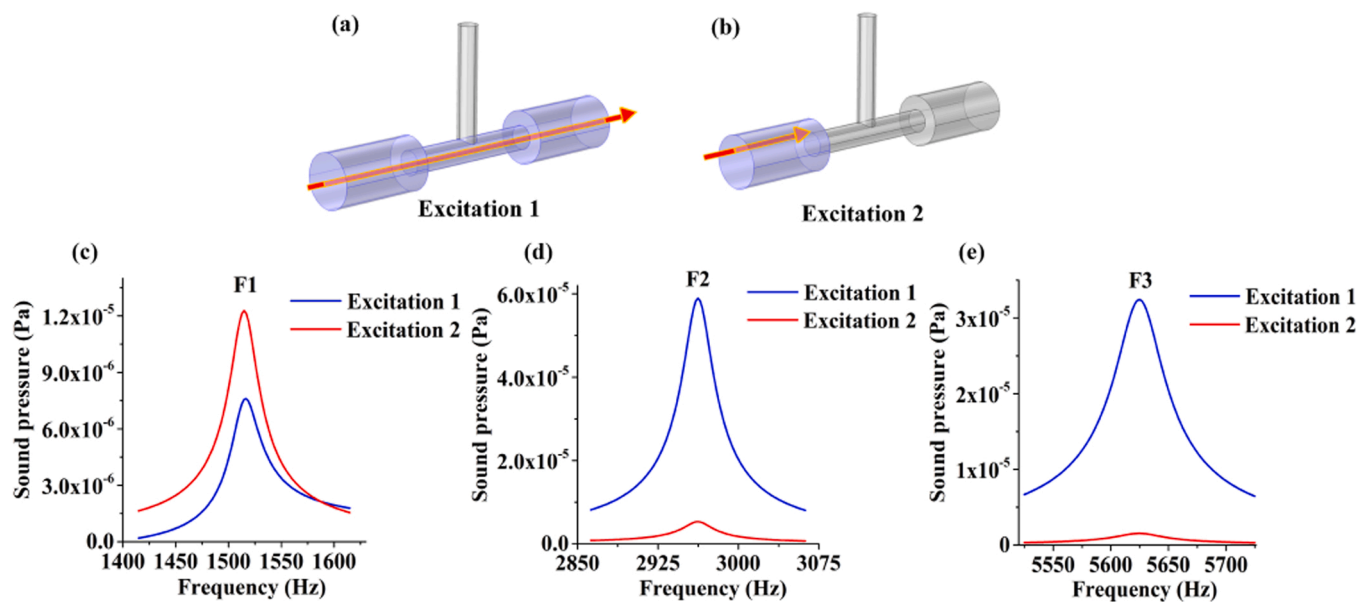


Fig. 4. Simulation results of the T-type PAC acoustic characteristics with the incident beam position optimization. (a) and (b): Two different incident ways of the excitation beam; (c), (d) and (e): The simulated pressure amplitude response vs. frequency for F1, F2 and F3 detection, respectively.

monitor flow rate and suppress pressure fluctuations. A humidity level of 2.42% within the gas line was tested in the outlet using a capacitive hygrometer (HonryTech Science and Technology Co., Ltd, model HT-LH362).

A high-sensitive microphone (BSWA, model MPA201, 51.2 mV/Pa) was inserted into the top of T-type PAC. Then the simultaneous detected PA signals were sent to three lock-in amplifiers (Stanford Research Systems, USA, model SR850) to be demodulated at the corresponding resonance frequencies of T-type PAC. The filter slope and time constant of the lock-in amplifiers were set to 12 dB/oct and 1 s, respectively, which corresponds to a 0.125 Hz detection bandwidth. The PAS measurements were carried out at a room temperature in the lab (22 °C) and a working pressure of 760 Torr.

4. Beam position optimization and resonant frequency responsiveness

After determining the gas samples and laser sources, a series of experiments can be performed to verify the incident beam position optimization and resonant frequency responses of T-type PAC. To show that the acoustic characteristics of T-type PAC are independent of changes in light sources and gas species, the gas samples of 100 ppm CO, 50 ppm CH₄ and 50 ppm C₂H₂ were tested successively using QCL, ICL and DFB

laser diode respectively. The experimental results of the PA signals for different resonance modes by scanning the incident excitation beam position are given in Fig. 6. The spot diameters of QCL source, ICL source and DFB laser diode were about 3 mm, 3.5 mm and 1.2 mm. The scanning steps of QCL and ICL for CH₄ was 0.5 mm, and that of DFB laser diode was 1 mm. As shown in Fig. 6(a), the beam was incident into the PAC in parallel, which scanned from the upper edge of the buffer cavity, to passing through the PAC, and finally to the lower edge of the buffer cavity. Fig. 6(b)–(d) show the PA signals of 100 ppm CO, 50 ppm CH₄ and 50 ppm C₂H₂ with beam scanning displacements. The PA amplitudes of F1 mode with the beam irradiating in the buffer cylinder are much greater than that with passing through absorption cylinder. Note that the F1 mode amplitudes of CO, CH₄ and C₂H₂ are 0.2307 mV, 0.033 mV and 0.0075 mV at 0 mm, and increase to 3.9599 mV, 0.203 mV and 0.045 mV at −7.5 mm, respectively. Nevertheless, the PA signals of F2 and F3 mode obtain the maximum amplitude with the beam passing through the absorption cylinder at 0 mm. The gradual changes and abrupt changes of curves in the three figures are caused by the different proportion of buffer and absorption cavity due to the spot sizes. For the QCL and the ICL with wide spot diameters, the amplitudes change slightly after deviation from the central axis, and the sudden changes occur when the part of beam is irradiated on the wall. Considering the signal enhancement of F1 mode and the interference

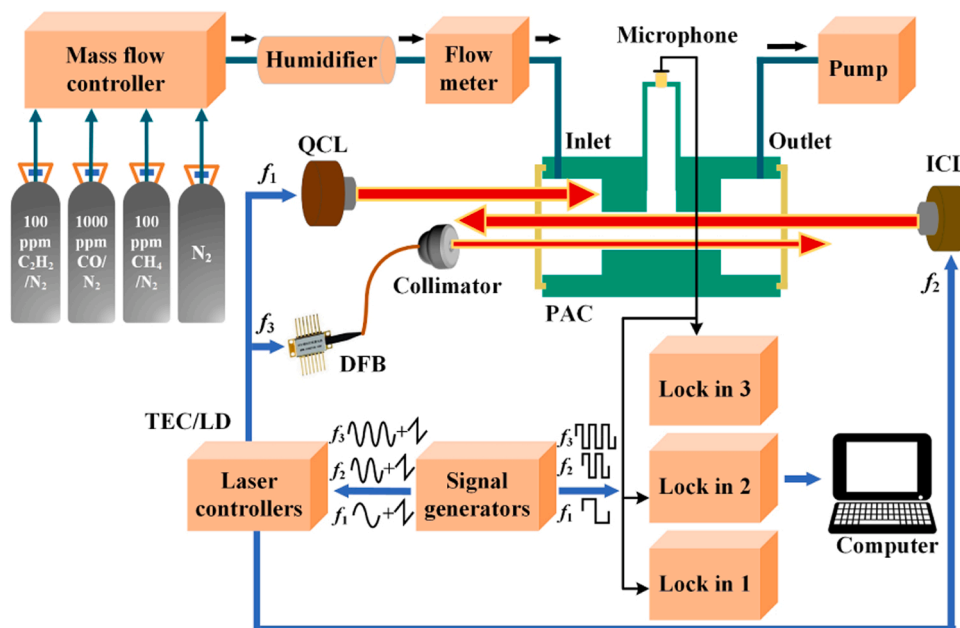


Fig. 5. The schematic diagram of multi-resonance PAS-based gas sensor configuration equipped with the developed T-type PAC for multi-component gas simultaneous detection. Operating pressure: 760 Torr.

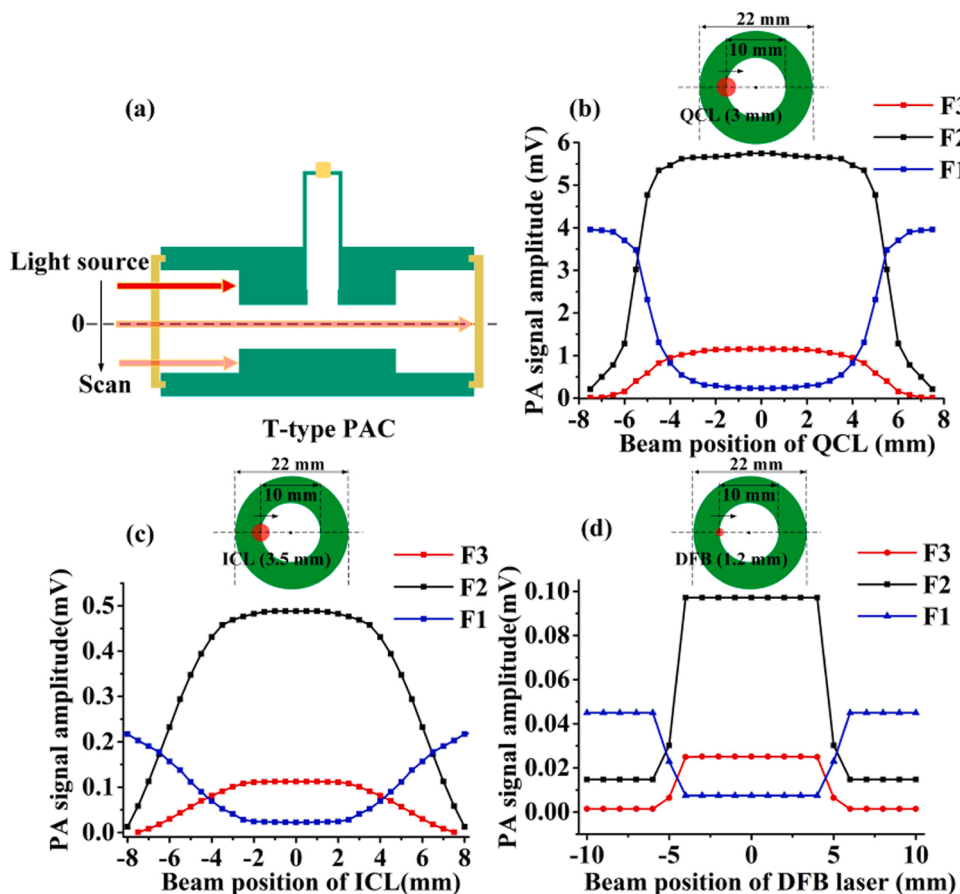


Fig. 6. The experimental results of PA signals for different resonance modes by scanning the incident excitation beam. (a) Schematic diagram of the light source scanning process in the T-type PAC. Dashed line: Central axis. (b) The PA amplitude of 100 ppm CO vs. the beam position of ICL source. (c) The PA amplitude of 50 ppm CH₄ vs. the beam position of ICL source. (d) The PA amplitude of 50 ppm C₂H₂ vs. the beam position of DFB laser. Insert: The irradiated surface of PAC.

among the beams to avoid direct relative irradiation, we finally determined that the beam positions of three lasers were -7.5 mm, -1 mm and 3.5 mm for QCL, ICL and DFB laser diode, respectively.

To further prove that the measured PA signals were the sound waves generated by the target gas molecules, rather than the thermal signal and background noise caused by the light beam irradiating on the buffer walls, a set of CH_4 detection experiments were implemented as shown in Fig. 7. Two different ways (I_1 , I_2) of incident beam were performed successively to excite the CH_4 molecules by ICL at different locations as shown in Fig. 7(a). The PA amplitude vs. frequency responses of F1 for the two incident ways are given in Fig. 7(b). The resonant frequencies of the PAC were scanned with a step of 1 Hz between 800 Hz and 1200 Hz. As a result, the maximum PA amplitudes were acquired at the same resonant frequency (1413 Hz) for both incidence ways, and the PA amplitudes of I_2 were greater than that of I_1 . By sending a 0.03 Hz ramp signal to the laser controller, the PA spectra of 100 ppm CH_4 in the ICL tuning range using both incidence ways are presented in Fig. 7(c). The amplitude is increased by a factor of 5 for the second incidence approach (from 0.067 mV to 0.406 mV). The PA signal amplitude responses with the concentrations of CH_4 for two incidence ways are given in Fig. 7(d). The concentration responses for both incidence ways showed the good linearities.

After determining the beam positions (-7.5 mm, -1 mm, and 3.5 mm for QCL, ICL, and DFB), the noise levels are shown in Fig. 8. For each of the three analytes, the noise level was estimated as the 1σ -fluctuation of the PA signal acquired while pure N_2 was flowing (400 sccm), and the sine-modulated injection current was fixed at absorption peak for the three lasers. These results show that the noise levels of I_2 are slightly larger than that of I_1 , which are resulted from laser interacting with buffer-cylinder walls and windows due to the light scattering and reflection. The change of irradiation modes causes a little effect on noise amplitudes. The noise levels of two incidence ways prove that the signal enhancement on F1 mode is generated by target gas molecules. Compared with the first approach, the SNR of PA signal for the second

incidence way was improved by 4.5 times. These experimental results demonstrated that the optimization of excitation beam position can improve the PA coupling degree and the detection sensitivity for F1 mode of T-type PAC without the maximum absorption optical path, which was consistent with the FEA simulation results. With rising the resonant frequency, the background noise and ambient noise and $1/f$ noise are suppressed more obviously. Due to the selection of three laser excitation modes, the noise levels were found to be $\sim 3.51\mu\text{V}$, $\sim 0.77\mu\text{V}$ and $\sim 0.334\mu\text{V}$ for F1, F2 and F3 detection, respectively.

Based on the above simulation and experimental results of T-type PAC, the resonant frequency responses in the range of 300–2000 Hz with a step of 1 Hz were finally measured by testing the 100 ppm CH_4/N_2 with ICL source. As shown in Fig. 9, there were three resonant frequencies for this developed PAC, corresponding to the F1, F2, and F3 respectively. This acoustic characteristic combined with the FDM technology is feasible and effective for simultaneously multi-component detection using a single resonator and a single microphone.

For the home-made T-type PAC used in the experiments, the tested resonant frequencies were about 1413 Hz (F1), 2912 Hz (F2) and 5310 Hz (F3), respectively. The Q factors and FWHMs of the resonance curves of F1, F2 and F3 can be calculated as $Q_1 = 21$, $\text{FWHM}_1 = 67$ Hz; $Q_2 = 43$, $\text{FWHM}_2 = 68$ Hz; and $Q_3 = 28$, $\text{FWHM}_3 = 192$ Hz. The blue shift occurred in the three resonant frequencies of home-made PAC, and the Q factors decreased compared with the simulation results. This phenomenon is mainly due to the machining errors during production. The materials used to make the PAC, the wall rigidity, and the changes in the acoustic velocity and the environmental factors can all contribute to these differences.

The highest signal amplitude can be achieved when the laser modulation amplitude is close to the absorption line width. Fig. 10 shows the relationship between the PA signals and modulation amplitude at 100 ppm CH_4 , 400 ppm CO and 100 ppm C_2H_2 . The optimal modulation amplitudes of ICL (CH_4), QCL (CO) and NIR laser diode (C_2H_2) resulted to be 55 mV, 1.5 V and 290 mV, respectively.

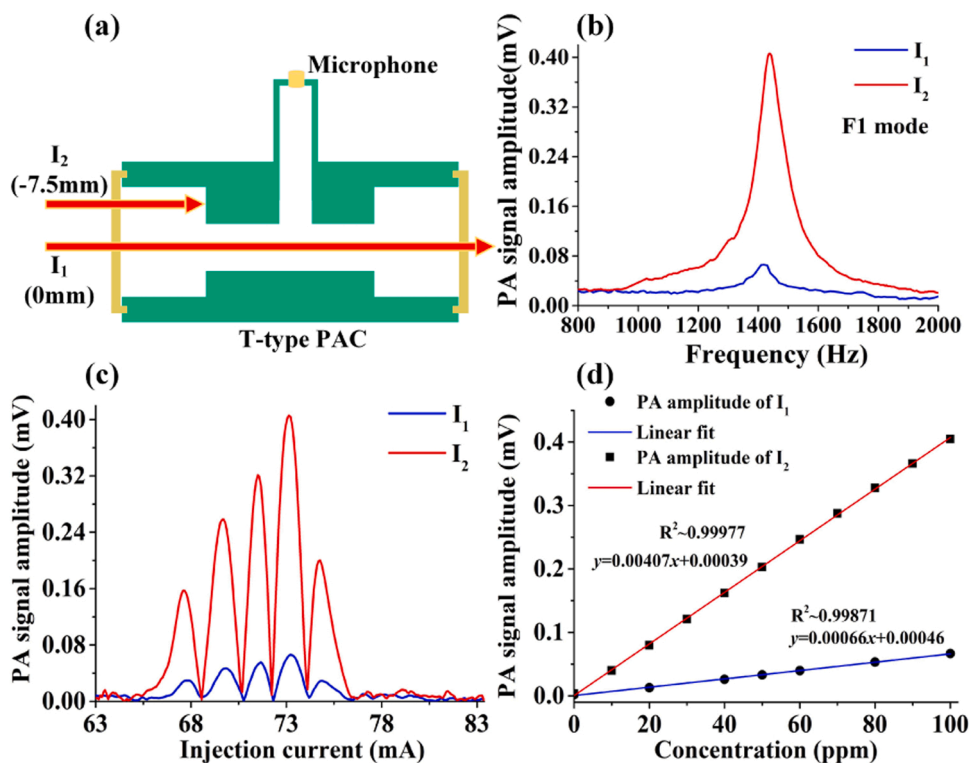


Fig. 7. The experimental results for CH_4 detection with the incident beam position optimization. (a) Two different ways (I_1 , I_2) of incident excitation beam using ICL for CH_4 measurement; (b) The PA amplitude vs. frequency of F1 for the two incident ways; (c) The PA spectra of 100 ppm CH_4 in the ICL tuning range using both incidence ways; (d) The PA signal amplitude of CH_4 vs. gas concentration for two incidence ways.

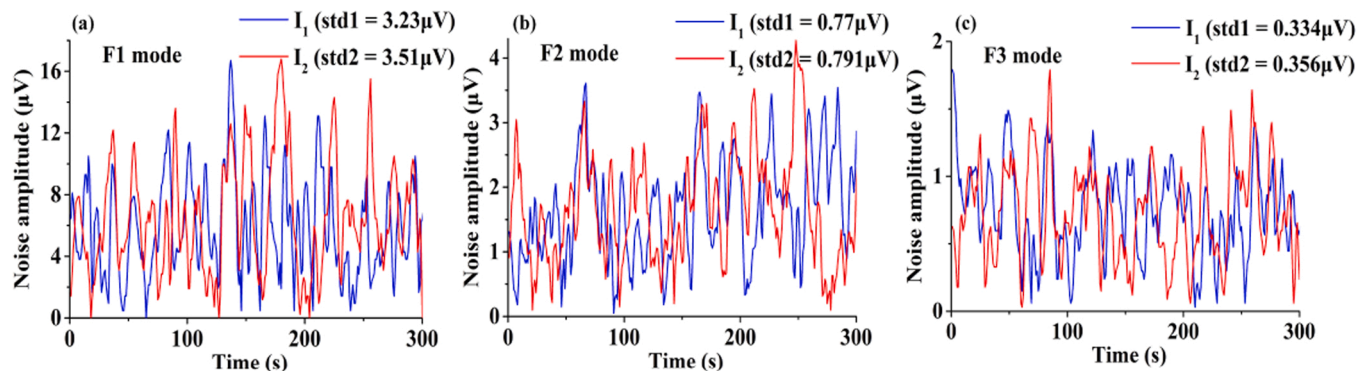


Fig. 8. Noise level analysis of F1, F2 and F3 modes for two incidence ways.

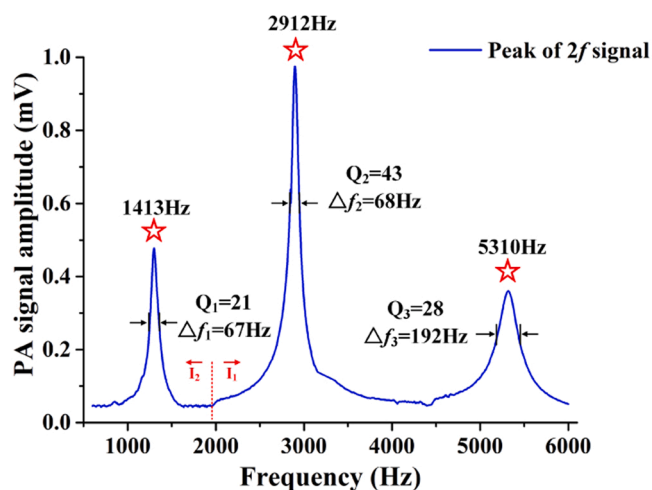


Fig. 9. Experimental frequency responses of the developed T-type PAC.

5. Multi-component gas sensing results and potential cross-sensitivity analysis

In case of multi-gas calibration experiments, the gas mixtures were diluted with highly purified N_2 by the mass flow controller. The three beams simultaneously transmitted into the PAC, and the mixed PA signals were demodulated using FDM technology. Fig. 11(a)-(c) show the

simultaneously measured PA spectra of $2f$ harmonic signal with different concentrations of CO , CH_4 and C_2H_2 , respectively.

As H_2O vapor can cause serious measurement errors in practical applications, the potential cross-sensitivities of humidity and mixed analytes need to be analyzed. This section is meant to further investigate the impact of H_2O , thus affecting the PA signal due to energy relaxation. The improved humidification system for humidity control is shown in Fig. 12. The used gas sample was the gas mixture of 100 ppm CO , 100 ppm CH_4 and 100 ppm C_2H_2 diluted in N_2 . To provide a defined humidification of the gas mixture, the gas path before entering the photoacoustic cell was divided into two parts by a 3-way valve including the humidification path and drying path. The humidification path passed through a humidifier with a fixed concentration of water (2.42%), and was then mixed with another drying path by a confluence valve. Both paths used a needle valve and a mass flow controller to jointly regulate the flow rates. The total flow rate after the mixed path was set to 400 sccm, so as to suppress the adsorption-desorption effect of H_2O . The total flow rate remains unchanged, which means that the flow rate 1 (drying path) + flow rate 2 (humidification path) = 400 sccm. By changing the flow rates of the two paths at the same time, the volume proportion of the H_2O to the total gas would be changed. This setup allows to change the humidity level, namely water vapor concentration. For example, if the flow rate 1 was set to 300 sccm and the flow rate 2 was set to 100 sccm, the concentration of H_2O vapor can be calculated as $100 \text{ sccm} / 400 \text{ sccm} * 2.42\% = 0.605\%$.

To verify the performance of the improved humidification system, a single 1392 nm DFB laser diode modulated on F2 mode was used in combination with a time division multiplexing approach to monitor the

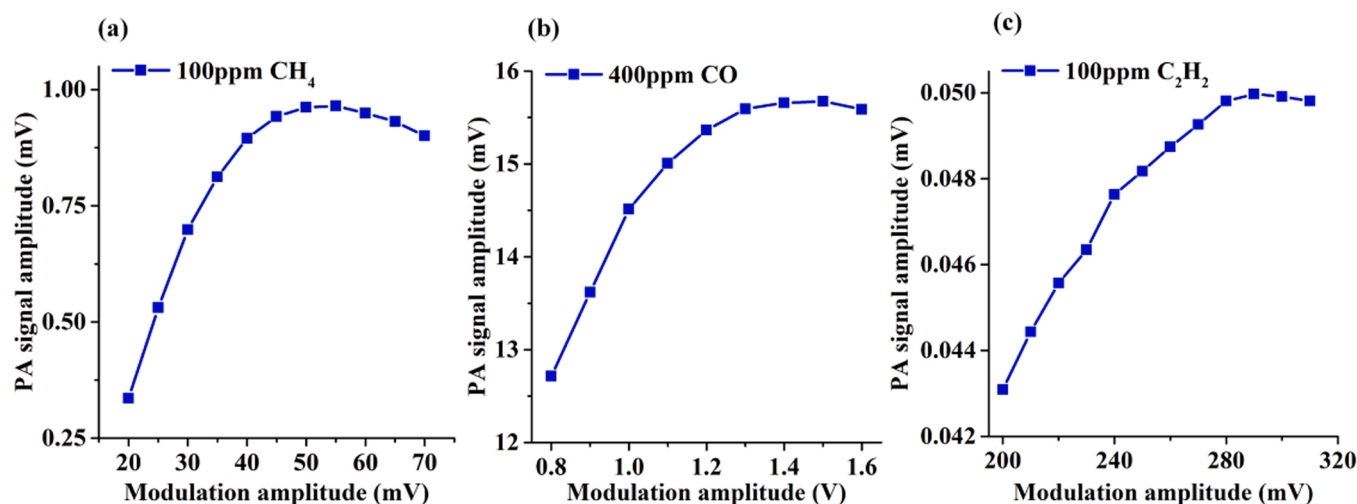


Fig. 10. The PA signal amplitudes vs. laser modulation amplitudes for multi-component gas sensing. (a) The ICL modulation amplitudes for 100 ppm CH_4 detection; (b) The QCL modulation amplitudes for 400 ppm CO detection; (c) The NIR laser diode modulation amplitudes for 100 ppm C_2H_2 detection.

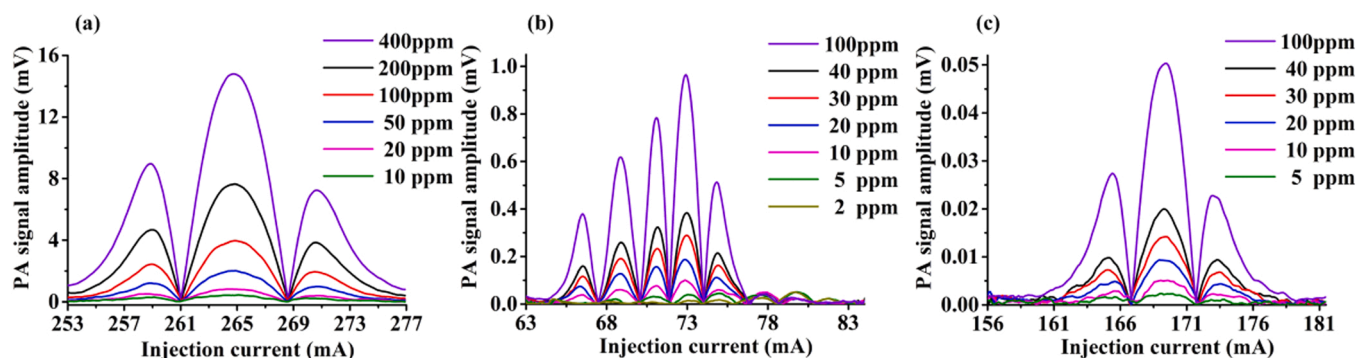


Fig. 11. The experimental results for simultaneous detection of multi-component gases. (a), (b) and (c): Measured 2f-PAS spectral scans of the CO, CH₄ and C₂H₂ absorption features for F1, F2 and F3 modes, respectively.

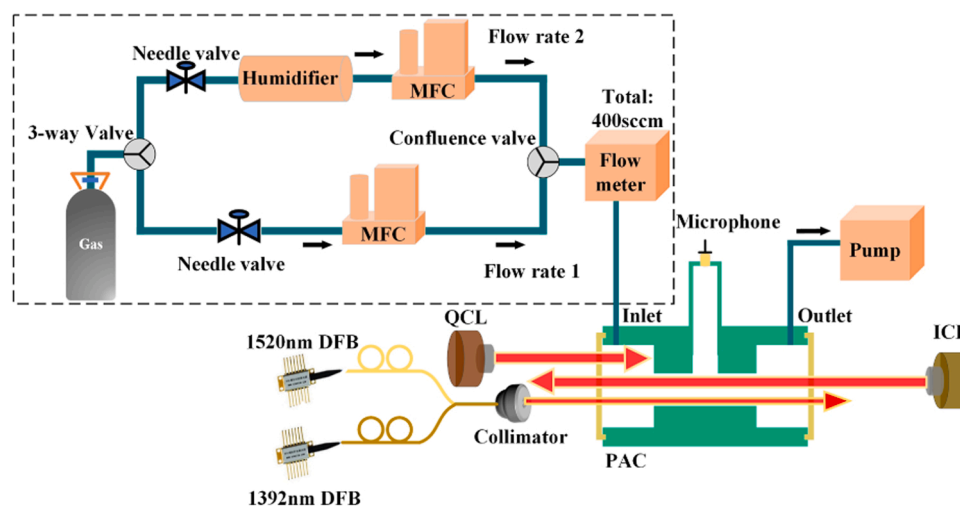


Fig. 12. Schematic of the improved humidification system for humidity control.

photoacoustic signal of water vapor. The recorded photoacoustic signal amplitude of the H₂O vapor vs. the humidity level (the proportion of flow rate) is given in Fig. 13. The Calibration curve shows a good linear concentration response of H₂O, which proves that the improved humidification system can be used to adjust the humidity level to study the energy relaxation characteristics of the other three target gases.

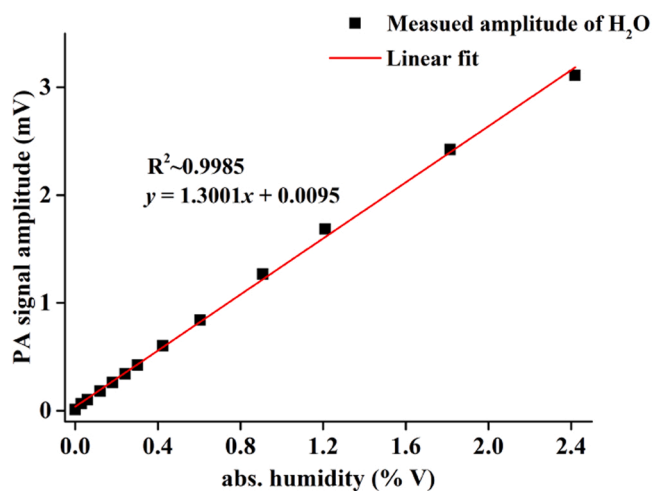


Fig. 13. Calibration curve of the measured amplitude of H₂O vs. the humidity level.

Through the above frequency division multiplexing (FDM) method, the relaxation characteristics of CO, CH₄ and C₂H₂ varying with the humidity level can be detected. The initial states were set as the results of drying measurement (i.e., flow rate 1 = 400sccm, flow rate 2 = 0). Next, humidity level was increased successively (the flow rate 2 was gradually increased while the flow rate 1 was gradually decreased), and the photoacoustic amplitudes were recorded after the 2f signals were stabilized.

The humidification results of a gas sample containing 100 ppm CO, 100 ppm CH₄ and 100 ppm C₂H₂ diluted in N₂ are presented respectively. As shown in Fig. 14, the photoacoustic amplitude of CO increased significantly by about 1.375 mV/%V-H₂O above 0.3025% humidity (flow rate 2 = 50sccm). The SNR at 2.42% humidity level is 8.4 times higher than that under dry conditions. This indicates that acceleration of relaxation causes the amplitude to increase. When the humidity level is lower than 0.3025%, the CO signal does not increase significantly due to its slow-relaxation. The result of CH₄ measurement is presented in Fig. 15. In the range of 0–0.1815% humidity level, the PA amplitude of CH₄ increases approximately linearly by 0.42 mV/%V-H₂O. This rise in amplitude is not only attributed to faster V-T relaxation of CH₄, but also to a fast V-V transition from CH₄ to H₂O with subsequent V-T relaxation of water. In the range of 0.1815–0.605% humidity level, the PA amplitude increases gradually and then reaches saturation. The highest CH₄ signal is 1.052 mV at 0.605% humidity level, an increase of 14% compared with the dry result of 0.9232 mV. With the humidity rises above 0.605%, the measured signal amplitude would decrease. The phenomenon of a decreasing amplitude by further humidification appears in both CH₄ and C₂H₂ measurements. Fig. 16 indicates the cross-

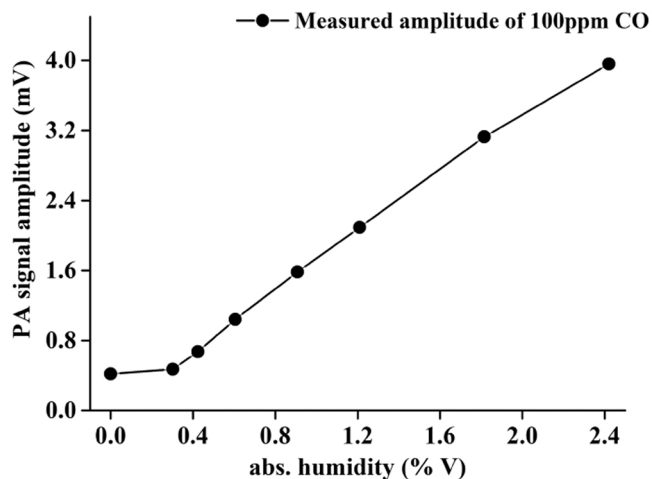


Fig. 14. Measured PA amplitude of 100 ppm CO with rising H_2O concentration.

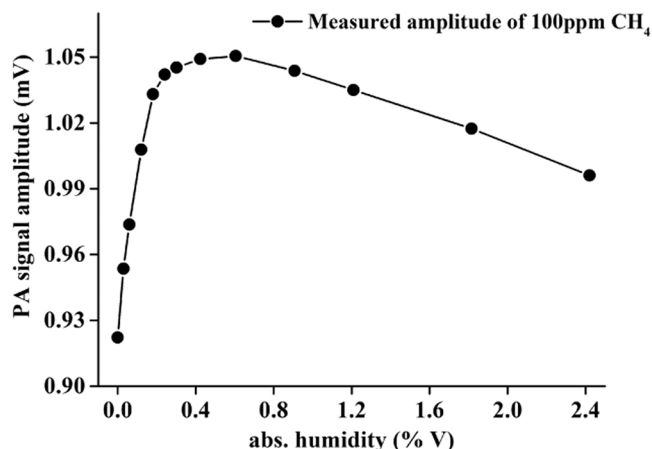


Fig. 15. Measured PA amplitude of 100 ppm CH_4 with rising H_2O concentration.

sensitivities of H_2O that might affect PA detection of C_2H_2 . With a decrease in PA amplitude which is analogous to previous CH_4 measurements by approx. $0.264\mu V/\%V-H_2O$ above 0.3025% humidity. This demonstrates that the fast relaxation molecule of C_2H_2 is almost not

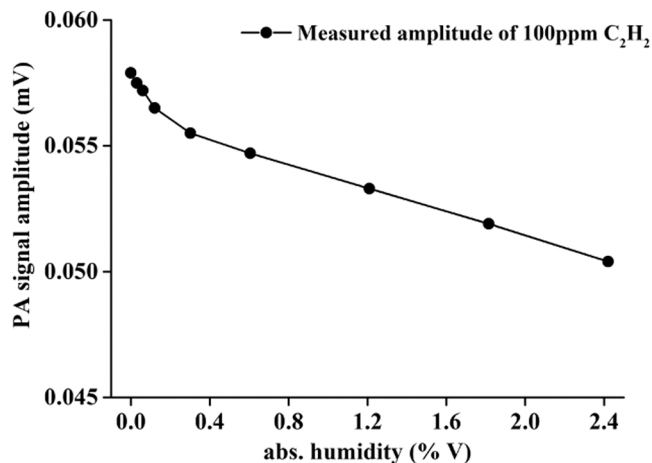


Fig. 16. Measured PA amplitude of 100 ppm C_2H_2 with rising H_2O concentration.

affected by the relaxation rate of water vapor. On the contrary, the rising H_2O concentration will cause the saturation effect and will change the specific heat ratio of the PAC, resulting in the decrease for PA signal [42].

Based on the above experimental results, we selected the humidity level of 2.42% as the final parameter of wet experiments, so as to realize the simultaneous measurement of three gases. Because the CO signal was significantly increased at 2.42% humidity, compared to the small increase for CH_4 signal and the less decrease for C_2H_2 signal. Simultaneous PAS measurement of wet CO, CH_4 and C_2H_2 based on multi-resonance modes compared with dry and humidified single-component measurement, were experimentally evaluated as shown in Figs. 17–19. Indeed, H_2O vapor has a high density of vibrational levels and fast relaxation rates, which creates multiple options for energy transfer in collisions with well-known slow-relaxation CO molecules. The presence of 2.42% H_2O vapor in gas samples strongly increases the PA signals from 0.42 mV to 3.96 mV, resulting in an 8.4 times improvement, compared with that of dry CO/ N_2 (blue curve in Fig. 17). The mixed CH_4 and C_2H_2 cause little spectral interference and relaxation effects on the PA spectra of wet CO, as the red and black curves almost overlapped. The spectral interference of H_2O on the PA spectra of CH_4 in the ICL tuning range of 75–80 mA is depicted in Fig. 18, which did not affect the peak signal. Due to the relaxation rate enhancement of H_2O , the PA signal was increased from 0.9232 mV to 0.9961 mV for dry and wet measurements. Fig. 19 shows that the peak amplitude of C_2H_2 signal drops from $57.9\mu V$ to $50.3\mu V$ because of the cross-sensitivity of H_2O . Any spectral impact on the peak amplitudes of target gases is not found in our PAS system.

6. Multi-gas calibration and detection limits

The linear response characteristics of the developed gas sensor were further evaluated with different sample concentrations compared with dry and wet measurements. The multi-component gas calibration results with different sample concentrations of CO, CH_4 and C_2H_2 are given in Figs. 20–22, respectively. By linear regression analysis, the corresponding regression coefficients R^2 for wet measurements were found to be 0.99957, 0.99983 and 0.99972, respectively. The regression coefficients R^2 for dry measurements were 0.9985, 0.9998 and 0.99979, respectively. Both results show the good linearity relationship. Therefore, the experimental calibration results were reliable for the mixed target gases humidified by the fixed concentration of H_2O vapor. Among them, the detection sensitivities of CO and CH_4 are increased by adding 2.42% H_2O vapor.

The SNRs of wet 100 ppm CO, 100 ppm CH_4 , and 100 ppm C_2H_2 are calculated to be 1128.5, 1246.6, and 150.6. The minimum detection limits (MDLs) (1σ), which are the concentrations at which the SNR is equal to 1, for each gas species, were evaluated as 89ppb for CO, 80ppb

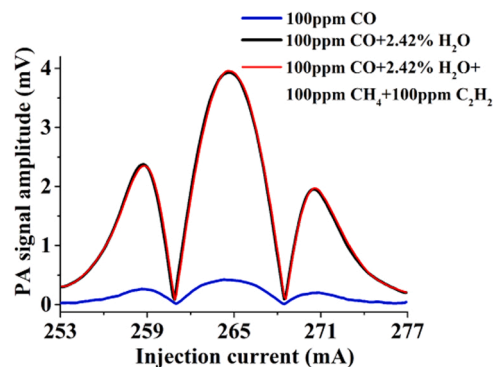


Fig. 17. Comparison of the measured PA spectra of CO for dry single-component, humidified target gas and multi-component simultaneous detection.

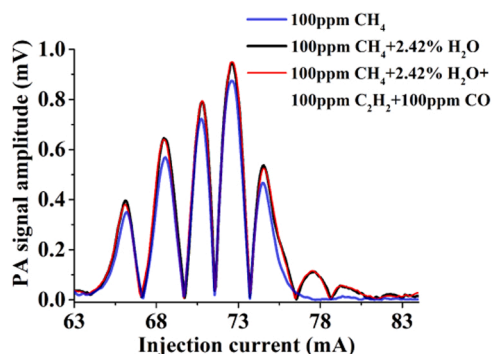


Fig. 18. Comparison of the measured PA spectra of CH₄ for dry single-component, humidified target gas and multi-component simultaneous detection.

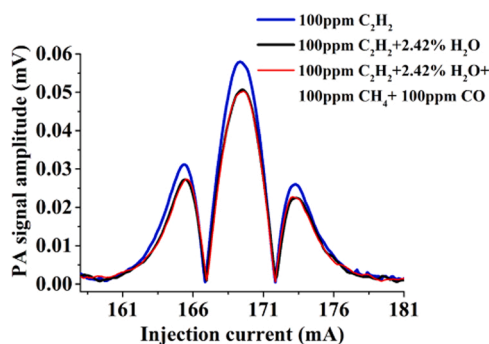


Fig. 19. Comparison of the measured PA spectra of C₂H₂ for dry single-component, humidified target gas and multi-component simultaneous detection.

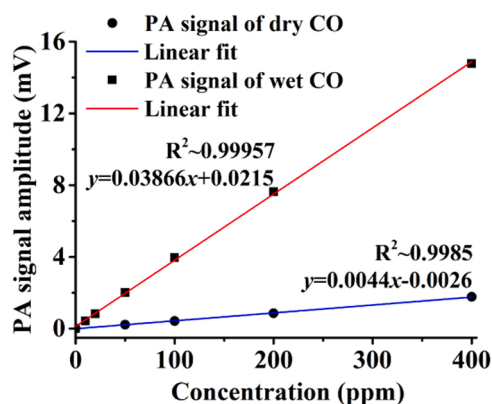


Fig. 20. Calibration curves of dry and wet CO for F1 detection.

for CH₄ and 664 ppb for C₂H₂, respectively. Taking into account the corresponding lasers powers, the normalized noise equivalent absorption (NNEA) coefficients of $5.75 \times 10^{-7} \text{ cm}^{-1} \text{ W Hz}^{-1/2}$, $1.97 \times 10^{-8} \text{ cm}^{-1} \text{ W Hz}^{-1/2}$ and $4.23 \times 10^{-8} \text{ cm}^{-1} \text{ W Hz}^{-1/2}$ were achieved for CO, CH₄ and C₂H₂ detection, respectively. In Table 1, a comparison was presented between the proposed T-type PAC-based multi-resonance system and previous PAS sensors. By comparing the MDLs and NNEA coefficients, the results reported in this work show competitive performance and better frequency responses on ppb-level multi-gas detection. The NNEA coefficient difference between CH₄ and C₂H₂ was much lower than the fundamental and overtone modes of QTF. For slow relaxation molecule of CO, the similar MDL were achieved compared with that of CH₄, with an integration time of 1 s

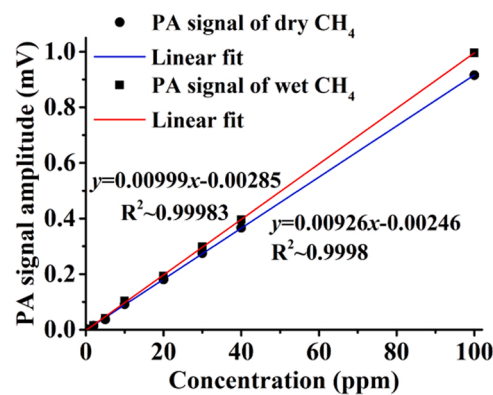


Fig. 21. Calibration curves of dry and wet CH₄s for F2 detection.

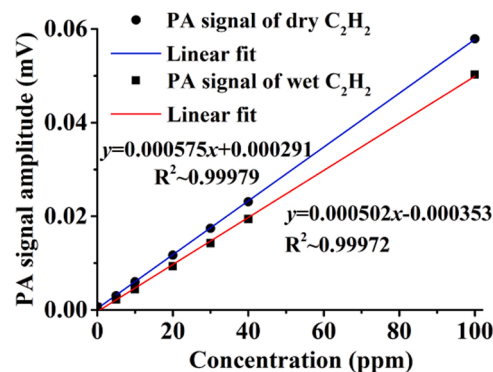


Fig. 22. Calibration curves of dry and wet C₂H₂ for F3 detection.

Thanks to the single T-type PAC and FDM method, the simultaneous measurement of CO, CH₄ and C₂H₂ based on the multiple resonance modes was achieved. Combined with the optimization of the incident excitation beam position, the multi-wavelength and multi-frequency scheme can improve the space utilization efficiency and simultaneous detection capability, resulting in a compact sensor for dissolved gas application.

7. Conclusions

A T-type cell based multi-resonance PAS gas sensor was established and verified to be capable of multi-component simultaneous ppb-level detection. By the FEA simulation optimization and experimental beam excitation position design, the PA responses of the three designated resonant frequencies are comparable which guarantees the high performance of multiple trace gas detection simultaneously. The three combustible species of CO, CH₄ and C₂H₂ were selected as target gases for the simultaneous detection verification using a QCL (4.59 μm , 44 mW), an ICL (3.37 μm , 8 mW) and a NIR laser diode (1.52 μm , 32 mW) as incident beams. The SNR for F1 mode with the beam irradiating on the buffer wall was increased by 4.5 times than that of passing through absorption cylinder. The experimental MDLs (1σ) were achieved as of 89 ppb (CO), 80 ppb (CH₄) and 664 ppb (C₂H₂) have been acquired, respectively, corresponding to the NNEA coefficients of $5.75 \times 10^{-7} \text{ cm}^{-1} \text{ W Hz}^{-1/2}$, $1.97 \times 10^{-8} \text{ cm}^{-1} \text{ W Hz}^{-1/2}$ and $4.23 \times 10^{-8} \text{ cm}^{-1} \text{ W Hz}^{-1/2}$. An improved humidification investigation regarding cross-sensitivity analysis provides a better understanding of PAS sensors in humidity relaxation related effects. This developed PAS modality of utilizing a single PAC and a single detector for multi-component gas sensing exhibits unique potential for early diagnosis of power transformer failures.

Table 1
Comparison of detection sensitivity performance with previous PAS publications.

Species	Wavelength (μm)	Power (mW)	Integration time	MDL	NNEA coefficient (cm ⁻¹ W Hz ^{-1/2})	Ref.
CO	1.567	< 1 mW	2.6 s	249.6 ppm	3.4×10^{-9}	[18]
CH ₄	1.617	< 1 mW		293.7 ppm	1.4×10^{-9}	
C ₂ H ₂	1.534	< 1 mW		1.5 ppm	3.6×10^{-9}	
CO	4.69	~15 [W] (broadband)	1 s	40 ppb	\	[21]
CH ₄	3.22	~15 [W] (broadband)		150 ppb		
C ₂ H ₂	1.533	15 mW		200 ppb		
CO	1.568	1000 (amplified by EDFA)	1 s	4.6 ppm	\	[23]
CH ₄	1.529	1000 (amplified by EDFA)		87 ppm		
C ₂ H ₂	1.532	1000 (amplified by EDFA)		1.3 ppb		
H ₂ O	1.368	21.2	300 ms	49 ppm	9.12×10^{-7}	[28]
C ₂ H ₂	1.529	10		11 ppm	1.51×10^{-7}	
H ₂ O	1.392	6.2	100 ms	20 ppm	\	[29]
CH ₄	7.707	128		18 ppb		
N ₂ O	7.71	128		5 ppb		
H ₂ O	1.396	7	181 s	1.17 ppm	6.03×10^{-10}	[30]
CH ₄	1.653	2.1	195 s	1.76 ppm	2.36×10^{-9}	
CO ₂	1.574	4	136 s	83 ppm	5.46×10^{-10}	
CO	4.59	44	1 s	89 ppb	5.3×10^{-7}	This paper
CH ₄	3.37	8		80 ppb	1.9×10^{-8}	
C ₂ H ₂	1.52	32		664 ppb	4.2×10^{-8}	

Declaration of Competing Interest

The authors declare that they have no known competing financial interests or personal relationships that could have appeared to influence the work reported in this paper.

Data availability

The authors are unable or have chosen not to specify which data has been used.

Acknowledgments

The authors are grateful to the National Natural Science Foundation of China (Grant Nos. 62175194, 62271370, and 62105252). This work was also supported by the Fundamental Research Funds for the Central Universities (Grant Nos. QTZX23081 and QTZX23069). We also acknowledge to the Concept Grant of Hangzhou Institute of Technology of Xidian University (No. GNYZ2023XJ0203). L. Liu acknowledges the Natural Science Foundation of Shaanxi Province (Grant No. 2023-YBSF-188). X.Y acknowledges the State Key Laboratory of Applied Optics on Changchun Institute of Optics (SKLAO2022001A12), the Natural Science Foundation of Shaanxi Province (2023-YBGY-099), and the Guangdong Basic and Applied Basic Research Foundation with Grant No. 2020A1515111012.

References

- [1] K. Chen, B. Zhang, M. Guo, H. Deng, B. Yang, Z. Gong, W. Peng, Q. Yu, All-optical photoacoustic multigas analyzer using digital fiber-optic acoustic detector, *IEEE Trans. Instrum. Meas.* 69 (10) (2020) 8486–8493.
- [2] Q. Wei, B. Li, B. Zhao, P. Yang, EC-QCL based photoacoustic spectroscopy for detection of SF₆ decomposition components, *Sens. Actuators B Chem.* 369 (2022), 132351.
- [3] C. Li, H. Qi, X. Zhao, M. Guo, R. An, K. Chen, Multi-pass absorption enhanced photoacoustic spectrometer based on combined light sources for dissolved gas analysis in oil, *Opt. Laser Eng.* 159 (2022), 107221.
- [4] S. Bustamante, M. Manana, A. Arroyo, P. Castro, A. Laso, R. Martinez, Dissolved gas analysis equipment for online monitoring of transformer oil: a review, *Sensors* 19 (2019) 4057.
- [5] A. Sampaolo, P. Patimisco, M. Giglio, A. Zifarelli, H. Wu, L. Dong, V. Spagnolo, Quartz-enhanced photoacoustic spectroscopy for multi-gas detection: a review, *Anal. Chim. Acta* 1202 (2022), 338894.
- [6] Y. Ma, S. Qiao, Y. He, Y. Li, Z. Zhang, X. Yu, F.K. Tittel, Highly sensitive acetylene detection based on multi-pass retro-reflection-cavity-enhanced photoacoustic spectroscopy and a fiber amplified diode laser, *Opt. Express* 27 (10) (2019) 14163–14172.
- [7] Y. Ma, R. Lewicki, M. Razezghi, F.K. Tittel, QEPAS based ppb-level detection of CO and N₂O using a high power CW DFB-QCL, *Opt. Express* 21 (1) (2013) 1008–1019.
- [8] S. Qiao, A. Sampaolo, P. Patimisco, V. Spagnolo, Y. Ma, Ultra-highly sensitive HCL-LITES sensor based on a low-frequency quartz tuning fork and a fiber-coupled multi-pass cell, *Photoacoustics* 27 (2022), 100381.
- [9] Z. Lang, S. Qiao, Y. He, Y. Ma, Quartz tuning fork-based demodulation of an acoustic signal induced by photo-thermo-elastic energy conversion, *Photoacoustics* 22 (2021), 100272.
- [10] X. Liu, S. Qiao, G. Han, J. Liang, Y. Ma, Highly sensitive HF detection based on absorption enhanced light-induced thermoelastic spectroscopy with a quartz tuning fork of receive and shallow neural network fitting, *Photoacoustics* 28 (2022), 100422.
- [11] Z. Wang, Q. Wang, H. Zhang, S. Borri, I. Galli, A. Sampaolo, P. Patimisco, V. Spagnolo, P.D. Natale, Wei Ren, Doubly resonant sub-ppt photoacoustic gas detection with eight decades dynamic range, *Photoacoustics* 27 (2022), 100387.
- [12] A. Zifarelli, R.D. Palo, P. Patimisco, M. Giglio, A. Sampaolo, S. Blaser, J. Butet, O. Landry, A. Müller, V. Spagnolo, Multi-gas quartz-enhanced photoacoustic sensor for environmental monitoring exploiting a Vernier effect-based quantum cascade laser, *Photoacoustics* 28 (2022), 100401.
- [13] G. Menduni, A. Zifarelli, A. Sampaolo, P. Patimisco, M. Giglio, N. Amoroso, H. Wu, L. Dong, R. Bellotti, V. Spagnolo, High-concentration methane and ethane QEPAS detection employing partial least squares regression to filter out energy relaxation dependence on gas matrix composition, *Photoacoustics* 26 (2022), 100349.
- [14] Y. Ma, Y. Hu, S. Qiao, Z. Lang, X. Liu, Y. He, V. Spagnolo, Quartz tuning forks resonance frequency matching for laser spectroscopy sensing, *Photoacoustics* 25 (2022), 100329.
- [15] X. Yin, H. Wu, L. Dong, B. Li, W. Ma, L. Zhang, W. Yin, L. Xiao, S. Jia, F.K. Tittel, Ppb-Level SO₂ photoacoustic sensors with a suppressed absorption–desorption effect by using a 7.41μm external-cavity quantum cascade laser, *ACS Sens.* 5 (2020) 549–556.
- [16] Y. Ma, Y. He, Y. Tong, X. Yu, F.K. Tittel, Quartz-tuning-fork enhanced photothermal spectroscopy for ultra-highly sensitive trace gas detection, *Opt. Express* 26 (24) (2018) 32103–32110.
- [17] Y. Ma, Y. Hu, S. Qiao, Y. He, F.K. Tittel, Trace gas sensing based on multi-quartz-enhanced photothermal spectroscopy, *Photoacoustics* 20 (2020), 100206.
- [18] E.D. McNaghten, K.A. Grant, A.M. Parkes, P.A. Martin, Simultaneous detection of trace gases using multiplexed tunable diode lasers and a photoacoustic cell containing a cantilever microphone, *Appl. Phys. B Lasers O* 107 (2012) 861–871.
- [19] L. Liu, A. Mandelis, H. Huan, K.H. Michaelian, Step-scan differential Fourier transform infrared photoacoustic spectroscopy (DFTIR-PAS): a spectral deconvolution method for weak absorber detection in the presence of strongly overlapping background absorptions, *Opt. Lett.* 42 (7) (2017) 1424–1427.
- [20] C.B. Hirschmann, J. Uotila, S. Ojala, J. Tenhunen, R.L. Keiski, Fourier transform infrared photoacoustic multicomponent gas spectroscopy with optical cantilever detection, *Appl. Spectrosc.* 64 (3) (2010) 293–297.
- [21] K. Chen, S. Liu, B. Zhang, Z. Gong, Y. Chen, M. Zhang, H. Deng, M. Guo, F. Ma, F. Zhu, Q. Yu, Highly sensitive photoacoustic multi-gas analyzer combined with mid-infrared broadband source and near-infrared laser, *Opt. Laser Eng.* 124 (2020), 105844.
- [22] X. Yin, L. Dong, H. Wu, L. Zhang, W. Ma, W. Yin, L. Xiao, S. Jia, F.K. Tittel, Highly sensitive photoacoustic multicomponent gas sensor for SF₆ decomposition online monitoring, *Opt. Express* 27 (4) (2019) A224–A234.
- [23] X. Mao, X. Zhou, Z. Gong, Q. Yu, An all-optical photoacoustic spectrometer for multi-gas analysis, *Sens. Actuators B Chem.* 232 (2016) 251–256.
- [24] Z. Wang, J. Chang, C. Tian, Y. Feng, C. Wang, H. Zhang, Q. Zhang, H. Li, Z. Feng, X. Zhang, L. Tang, Two-component gas quartz-enhanced photoacoustic

spectroscopy sensor based on time-division multiplexing of distributed-feedback laser driver current, *Appl. Opt.* 58 (31) (2019) 8479–8485.

- [25] K. Liu, J. Mei, W. Zhang, W. Chen, X. Gao, Multi-resonator photoacoustic spectroscopy, *Sens. Actuators B Chem.* 251 (2017) 632–636.
- [26] L. Zhang, L. Liu, H. Huan, X. Yin, X. Zhang, A. Mandelis, X. Shao, Non-local patch regression algorithm-enhanced differential photoacoustic methodology for highly sensitive trace gas detection, *Chemosensors* 9 (2021) 268.
- [27] Y. Cao, K. Liu, R. Wang, W. Chen, X. Gao, Three-wavelength measurement of aerosol absorption using a multi-resonator coupled photoacoustic spectrometer, *Opt. Express* 29 (2) (2021) 2258–2269.
- [28] H. Wu, X. Yin, L. Dong, et al., Simultaneous dual-gas QEPAS detection based on a fundamental and overtone combined vibration of quartz tuning fork, *Appl. Phys. Lett.* 110 (2017), 121104.
- [29] A. Elefante, M. Giglio, A. Sampaolo, G. Menduni, P. Patimisco, V.M.N. Passaro, H. Wu, H. Rossmadl, V. Mackowiak, A. Cable, F.K. Tittel, L. Dong, V. Spagnolo, Dual-gas quartz-enhanced photoacoustic sensor for simultaneous detection of methane/nitrous oxide and water vapor, *Anal. Chem.* 91 (2019) 12866–12873.
- [30] Q. Huang, Y. Wei, J. Li, Simultaneous detection of multiple gases using multi-resonance photoacoustic spectroscopy, *Sens. Actuators B Chem.* 369 (2022), 132234.
- [31] I.E. Gordon, L.S. Rothman, R.J. Hargreaves, et al., The HITRAN2020 molecular spectroscopic database, *J. Quant. Spectrosc. Radiat. Transf.* 277 (2022), 107949.
- [32] A. Miklos, P. Hess, Application of acoustic resonators in photoacoustic trace gas analysis and metrology, *Rev. Sci. Instrum.* 72 (4) (2001) 1937–1955.
- [33] L. Liu, H. Huan, W. Li, A. Mandelis, Y. Wang, L. Zhang, X. Zhang, X. Yin, Y. Wu, X. Shao, Highly sensitive broadband differential infrared photoacoustic spectroscopy with wavelet denoising algorithm for trace gas detection, *Photoacoustics* 21 (2020), 100228.
- [34] Z. Gong, K. Chen, Y. Chen, L. Mei, Q. Yu, Integration of T-type half-open photoacoustic cell and fiber-optic acoustic sensor for trace gas detection, *Opt. Express* 27 (13) (2019) 18222–18231.
- [35] Z. Gong, T. Gao, L. Mei, K. Chen, Y. Chen, B. Zhang, W. Peng, Q. Yu, Ppb-level detection of methane based on an optimized T-type photoacoustic cell and a NIR diode laser, *Photoacoustics* 21 (2021), 100216.
- [36] H. Xiao, J. Zhao, C. Sima, P. Lu, Y. Long, T. Ai, W. Zhang, Y. Pan, J. Zhang, D. Liu, Ultra-sensitive ppb-level methane detection based on NIR all-optical photoacoustic spectroscopy by using differential fiber-optic microphones with gold-chromium composite nanomembrane, *Photoacoustics* 26 (2022), 100353.
- [37] L. Liu, H. Huan, A. Mandelis, L. Zhang, C. Guo, W. Li, X. Zhang, X. Yin, X. Shao, D. Wang, Design and structural optimization of T-resonators for highly sensitive photoacoustic trace gas detection, *Opt. Laser Technol.* 148 (2022), 107695.
- [38] J.M. Rey, M.W. Sigrist, New differential mode excitation photoacoustic scheme for near-infrared water vapour sensing, *Sens. Actuators B Chem.* 135 (2008) 161–165.
- [39] J.M. Rey, M.W. Sigrist, Differential mode excitation photoacoustic spectroscopy: a new photoacoustic detection scheme, *Rev. Sci. Instrum.* 78 (2007), 063104.
- [40] J.M. Rey, C. Romer, M. Gianella, M.W. Sigrist, Near-infrared resonant photoacoustic gas measurement using simultaneous dual-frequency excitation, *Appl. Phys. B Lasers O* 100 (2010) 189–194.
- [41] K. Song, H.K. Cha, V.A. Kapitanov, Y.U.N. Ponomarev, A.P. Rostov, D. Courtois, D. Courtois, B. Parvitte, V. Zeninari, Differential Helmholtz resonant photoacoustic cell for spectroscopy and gas analysis with room-temperature diode lasers, *Appl. Phys. B Lasers O* 75 (2002) 215–227.
- [42] J. Pangerl, M. Muller, T. Ruck, S. Weigl, R. Bierl, Characterizing a sensitive photoacoustic sensor for multiple hydrocarbon gas detection considering changing ambient parameters and bulk composition (N₂, O₂ and H₂O), *Sens. Actuators B Chem.* 352 (2022), 130962.



Lixian Liu received her B.S. degree of electronic science and technology and doctorate of optical engineering from University of Electronic Science and Technology of China, in 2012 and 2017 respectively. She is now a full-time associate professor in School of Physics and Optoelectronic Engineering in Xidian University. Her research field is photoacoustic and optical spectroscopic technology.



Xueshi Zhang is a Ph.D. student at the School of Physics and Optoelectronic Engineering, Xidian University. He focuses on the high sensitivity trace gas detection technology and compact photoacoustic system design.



Xukun Yin received his Ph.D. degree in atomic and molecular physics from Shanxi University, China, in 2020. From 2018–2019, he studied as a research associate in the electrical and computer engineering department, Rice University, Houston, USA. Currently he is an associate professor in the School of Physics and Optoelectronic Engineering of Xidian University. His research interests include optical sensors, laser spectroscopy techniques and insulation fault diagnosis of electrical equipment.



Huiting Huan received his B.S. and Ph.D. degrees from University of Electronic Science and Technology of China in 2012 and 2017 respectively. He is now a researcher and lecturer with the School of Mechano-Electronic Engineering, Xidian University. His main research field includes acoustic, electromagnetic and thermal radiometric non-destructive testing.



Le Zhang is a Ph.D. student at the School of Physics and Optoelectronic Engineering, Xidian University. He received his B. S. degree from Xidian University in 2017. His research interests include photoacoustic spectroscopy and its application in trace gas detection.



Huanyu Liu is a graduate student at the School of Physics and Optoelectronic Engineering, Xidian University. Her focuses on the multi-pass cell design and highly sensitive trace gas detection technology.



Xiaoming Zhao received his Ph.D. degree from Xidian University. He is a professor at the School of Physics and Optoelectronic Engineering, Xidian University. His research focuses on the embedded system design and development, signal processing, and computer vision object detection, recognition and tracking technology.



Yufei Ma received his Ph.D. degree in physical electronics from Harbin Institute of Technology, China, in 2013. From September 2010 to September 2011, he spent as a visiting scholar at Rice University, USA. Currently, he is a professor at Harbin Institute of Technology, China. He is the winner of National Outstanding Youth Science Fund. His research interests include optical sensors, trace gas detection, laser spectroscopy, solid-state laser and optoelectronics. He has published more than 100 publications and given more than 20 invited presentations at international conferences. He serves as associate editor for *OSA Optics Express*, *SPIE Optical Engineering* and *Wiley Microwave and Optical Technology Letters*. He also serves as topical editor for *CLP Chinese Optics Letters* and editorial board member for Elsevier *Photoacoustics* and *MDPI Sensors*.



Xiaopeng Shao received his Ph.D. degree from Xidian University in 2005. He is a professor at the School of Physics and Optoelectronic Engineering, Xidian University. His research focuses on the computational imaging, optical sensing and signal processing.